J Mater Sci: Mater Electron (2020) 31:22252–22264

Fabrication of dandelion clock-inspired preparation of core-shell $TiO_2@MoS_2$ composites for unprecedented high visible light-driven photocatalytic performance

G. Mahalakshmi[1,*], M. Rajeswari[1], and P. Ponnarasi[1]

[1] *PG and Research Department of Physics, Government Arts College (Autonomous) (Affiliated to Bharathidasan University), Karur 639005, Tamilnadu, India*

Received: 1 June 2020
Accepted: 20 October 2020

ABSTRACT

Phase junction construction and surface modification are two practical engineering strategies toward efficient photocatalysis. In the present work, core-shell $TiO_2@MoS_2$ heterojunction composites were directly constructed via one-step hydrothermal method. The prepared catalysts are characterized by X-ray diffraction, Raman spectroscopy, Scanning electron microscopy, Transmission electron microscopy, and N_2 adsorption–desorption studies to know the structural, morphological, and textural properties. The optical absorption and prevention of electron–hole recombination process was studied by UV–Vis diffuse reflectance spectra (DRS) and photoluminescence analysis. The photocatalytic degradation experiment was carried out using methyl orange (MO) and 4-nitrophenol (4-NP) for all the catalysts under visible light irradiation. The results reveal that $MoS_2@TiO_2$ heterojunction catalyst shows excellent photocatalytic activity toward 4-NP such as high removal efficiency (96%), high apparent constant (0.0242 min^{-1}), and long-term stability. The enhancement in the photodegradation is due to dandelion clock heterostructures of $MoS_2@TiO_2$ possess high specific surface area (103.5 m^2/g), specific pores (11.8 nm). The photoelectrochemical results suggest that $MoS_2@TiO_2$ catalyst exhibits the high photoresponse than compared with pure MoS_2 and TiO_2 catalysts, respectively.

1 Introduction

With the rapid growth of economy and global industrialization, pollutions especially airborne ones have become one of the most severe threats facing humanity. In the practical scenario, air pollutants are highly complicated and can be generally described as particles, liquid droplets, gases, or mixtures of the above. Semiconductor heterostructure is an important strategy to improve the electrical properties such

---

Address correspondence to E-mail: arunaamaha@gmail.com

https://doi.org/10.1007/s10854-020-04726-4

as separation efficiency of carries. In this heterostructure, the energy band structures of component semiconductors are convenient for electrons and holes transferring through the interface between the heterostructure results in a longer carrier lifetime. This approach has been widely employed in transistors, solar energy cells, as well as modified photocatalysts. Photocatalysts can transform solar energy to electrochemical or chemical energy which can be applied in pollution degradation and hydrogen production. The energy transfer efficiency of solar relies on the separation rate of photoinduced electrons and holes [1–19]. Recently, various semiconducting metal oxides (SnO_2, WO_3, ZnO and NiO) are effectively used as novel photocatalyst to degradation of various toxic pollutants [20].

Among these, titanium oxide (TiO_2), as one of capable semiconductor photocatalysts, has been extensively investigated for pollutant degradation [21], solar cells [22], photoelectrochemical electrodes [23] and other photocatalytic applications [24] because of its no harmfulness, high physical and chemical stability [25]. However, the large-scale application of industrial wise is further restricted due to their wide bandgap energy (3.2 eV for anatase) and rapid recombination of electron–hole pair, which affect the photochemical reaction of the bare TiO_2 [26–28]. Thus, suggesting sensible approaches to reduction of the bandgap and restraining the recombination of photogenerated electron–hole pairs are crucial to improve the photocatalytic ability of the material. Generally, doping with metals or composites with metal oxides or polymer or carbonaceous materials are suitable process to improve the photocatalytic activity of bare TiO_2. Particularly, MoS_2 as a typical layered transition metal sulfide with a structure composed of three stacked atom layers (S-Mo-S) has been a focus of research for long time because of narrow bandgap, wonderful morphologies, and extensive application including lithium batteries, hydrogen production, and photocatalysis. [29–32]. Besides, MoS_2 can also accept electrons and act as active sites for photocatalysis responses [33]. We believe that combination of TiO_2 with MoS_2 heterostructure is an ideal carrier's exchange channel to expand the separation time of photoinduced carriers and improve photocatalytic activity. Moreover, hole transfer is permitted from TiO_2 to MoS_2, thus reducing TiO_2 photocorrosion. The incorporated MoS_2 could reduce the bandgap energy as well as prevent the recombination of electron–hole pair, which results in high photocatalytic performance. Herein, we designed a facile synthesis of core-shell MoS_2@TiO_2 heterostructure with MoS_2 nanoflakes on TiO_2 nanospheres by a simple hydrothermal approach. To the best of our knowledge, there was no previous report about high-efficient 4-NP decomposition of MoS_2@TiO_2 heterostructure photocatalyst under visible light. This is the first report about high-performance visible light induced 4-NP decomposition by MoS_2@TiO_2 heterostructure photocatalyst synthesized by facile and one-pot hydrothermal approach.

2 Experimental procedure

2.1 Preparation of TiO_2 nanospheres

Initially, 10 ml of acetylacetone was mixed with 25 ml of isopropyl alcohol (IPA) under strong magnetic stirring. Then, titanium isopropoxide (TTIP, 5 ml) was quickly added to the above mixed solution, followed by strong stirring for 10 min. Then the resultant reaction was placed to a 50 mL Teflon autoclave. The hydrothermal reaction was carried out at 180 °C for 12 h. After cooled to room temperature, the final precipitate was centrifuged and washed with ethanol several times to remove the impurities and finally dried in a vacuum oven at 80 °C for 12 h for the further use. This final product was TiO_2 nanospheres.

2.2 Synthesis of core-shell MoS_2@TiO_2 composites

At first, 0.3 g of $Na_2MoO_4 \cdot 2H_2O$ was mixed with 0.4 g of thiourea in 50 ml of DI water under strong magnetic stirring for 30 min. Then 0.1 g of the as-synthesized TiO_2 nanopowder was mixed with the above-mentioned solution and stirred for 30 min. Then the resultant suspension was transferred to a 50 mL Teflon autoclave. The hydrothermal reaction was carried out at 180 °C for 12 h. Then, the autoclave was cooled down to room temperature. The resulting product was collected by centrifugation and washed several times with distilled water and ethanol followed by drying at 80 °C for 12 h using vacuum oven. For comparison, pure MoS_2 was synthesized under the similar condition without the presence of the TiO_2 nanospheres. The schematic representation of the synthesis procedure and photocatalytic setup is shown in Fig. 1a and b.

3 Results and discussion

3.1 Powder X-ray diffraction (XRD) analysis

XRD analysis was taken to know the structural and crystallographic information of the samples. Figure 1c shows the powder XRD pattern of MoS_2, TiO_2, and $MoS_2@TiO_2$ core-shell composite samples, respectively. The intense diffraction planes of (002), (101), (102), (103) and (110) are situated with equivalent 2θ of 14.22, 33.47, 36.22, 39.23 and 59.64°, which can be indexed to the hexagonal crystalline structure of MoS_2 (JCPDs card No.37–1492). Bare TiO_2 is exposed to the anatase phase due to the presence of following miller indices such as (101), (004), (200), (105), (204) and the results are in good accordance with the standard value (JCPDs card No.21–1272). The co-existence of both MoS_2 and TiO_2-related peaks in the composite sample is due to the combination of heterojunction between the MoS_2 and TiO_2 crystal matrix. Debye–Scherrer's equation was used to calculate the crystallite size of the samples and found to be 12, 19, and 26 nm for MoS_2, TiO_2, and $MoS_2@TiO_2$ core-shell composite samples, respectively [34].

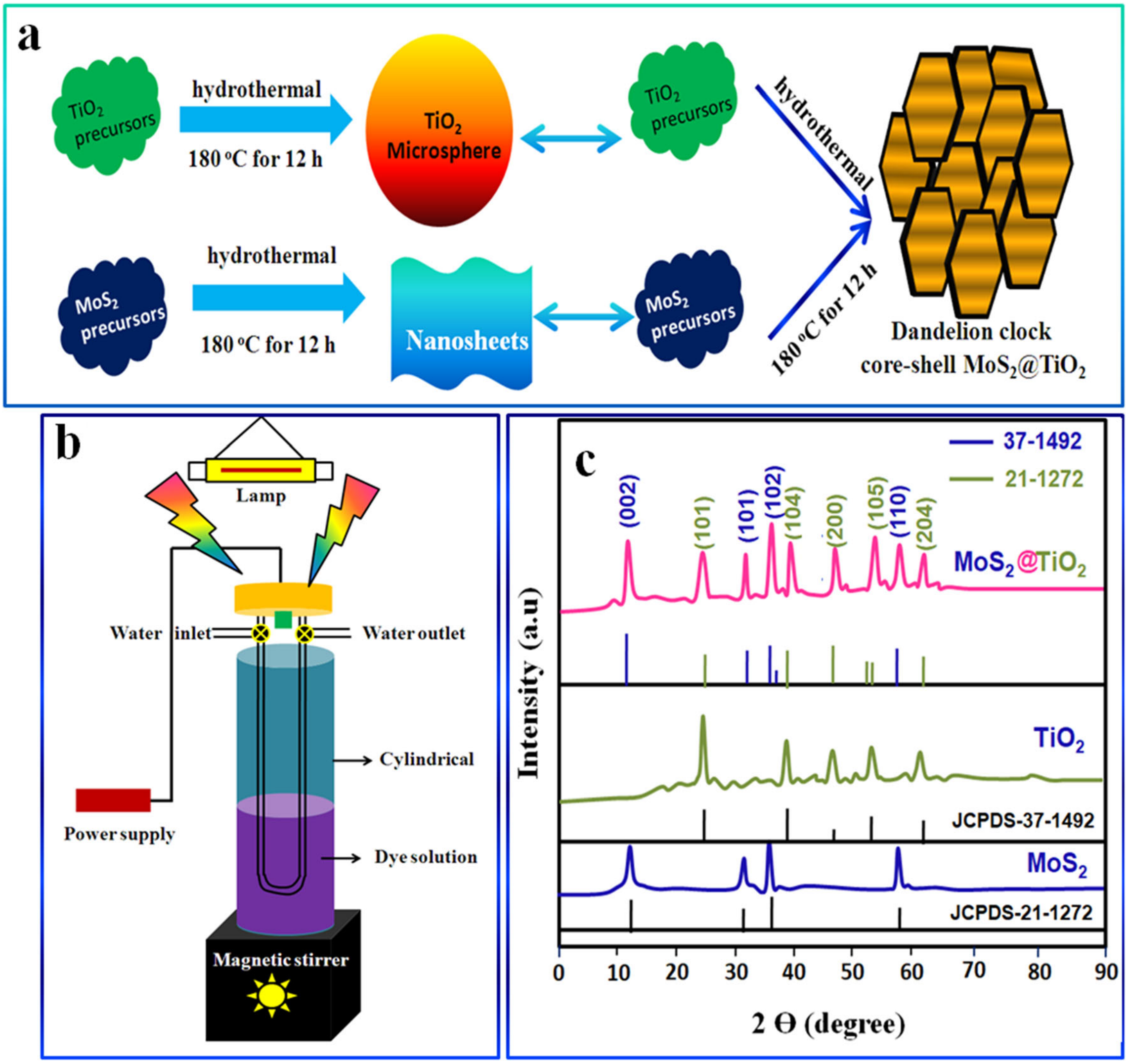

Fig. 1 (**a**) Schematic representation of the formation of $MoS_2@TiO_2$ heterostructure; (**b**) schematic representation of the photocatalytic setup; (**c**) XRD pattern of MoS_2, TiO_2 and $MoS_2@TiO_2$ composite samples

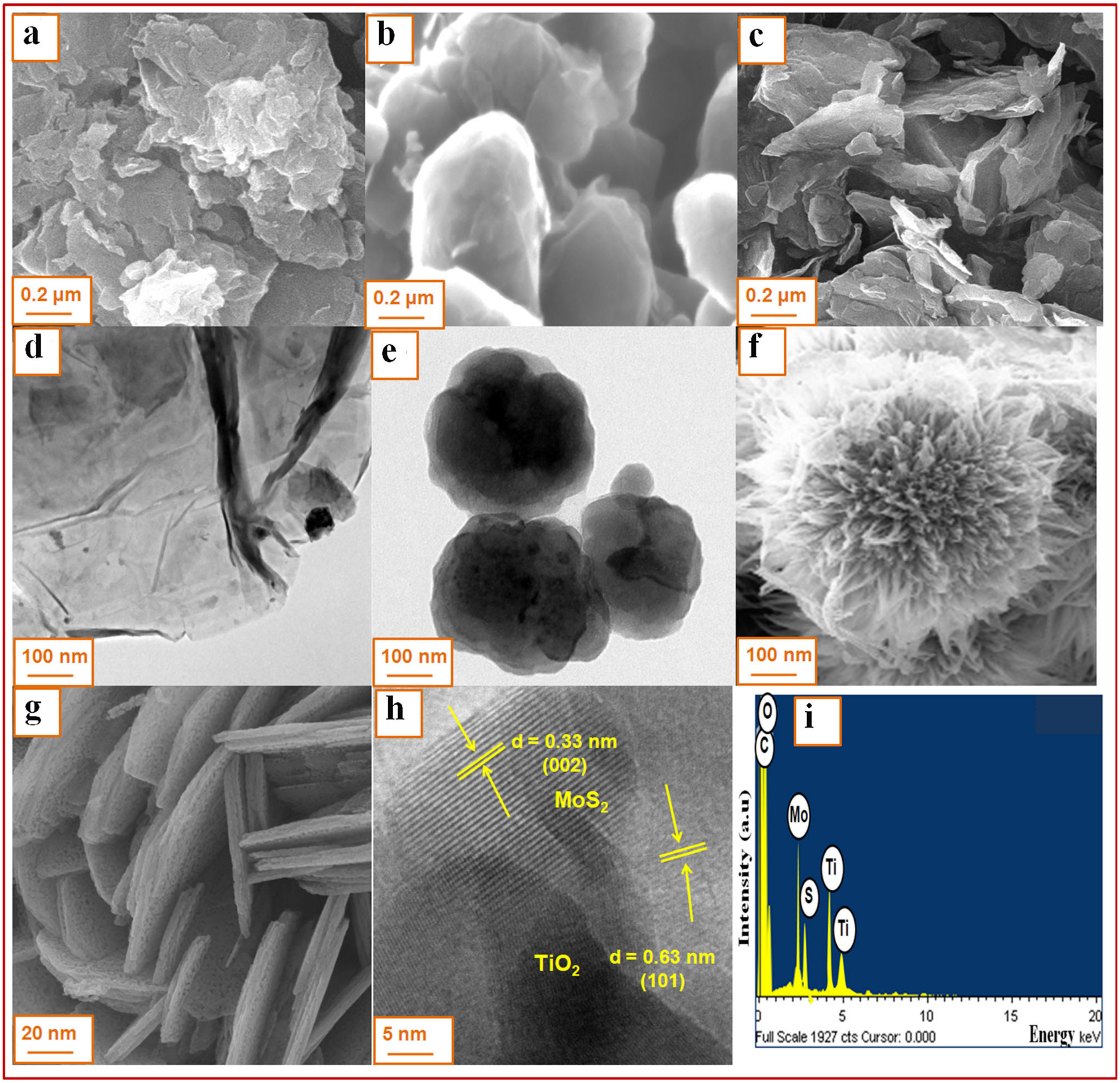

Fig. 2 SEM images of (**a**) MoS_2; (**b**) TiO_2; (**c**) MoS_2@TiO_2; TEM images of (**d**) MoS_2; (**e**) TiO_2; (**f**) & (**g**) MoS_2@TiO_2; (**h**) HRTEM image of MoS_2@TiO_2; (**i**) EDAX spectra of MoS_2@TiO_2

3.2 Morphological analysis

Figure 2a, b and c shows the SEM images of bare MoS_2, TiO_2 and MoS_2@TiO_2 core-shell composite samples, respectively. The pristine MoS_2 shows thin nanosheets structure (Fig. 2a), while the pristine TiO_2 displays sphere-like morphology (Fig. 2b). The MoS_2@TiO_2 composite sample consists of numerous nanoflakes, which is composed of spheres and sheets (Fig. 2c). TEM analysis was further confirmed the detailed sheets, spheres and core-shell structure of the samples. The clear nanosheets with wrinkle-type structure with monodispersed hollow spheres are observed in the MoS_2 (Fig. 2d) and TiO_2 (Fig. 2e) samples, respectively. Figure 2f and g shows the MoS_2@TiO_2 composite sample, which is clearly indicates that 3D hierarchical flower-like nanostructures. Further the HRTEM image shows two clearly crystal lattice fringes of 0.63 and 0.33 nm that can be indexed to the (101) planes of TiO_2 and (002) planes of MoS2

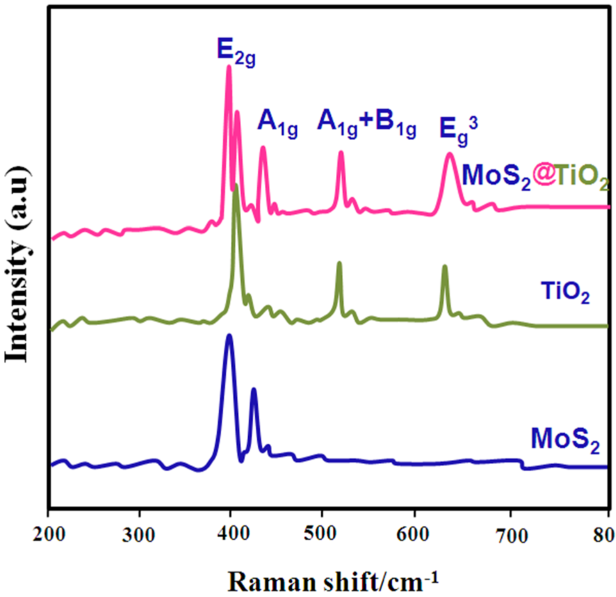

Fig. 3 Raman spectra of MoS_2, TiO_2 and $MoS_2@TiO_2$ composite samples

(Fig. 2h). The corresponding EDAX spectra again prove the formation of heterojunction due to the existence of chief elements such as Mo, S, Ti and O (Fig. 2i).

3.3 Raman spectra analysis

The heterojunction composite structure was further identified by the Raman spectroscopy and corresponding Raman spectra is shown in Fig. 3. Two Raman scattering peaks were identified at 390 and 418 cm^{-1} which is due to the E_{2g} and A_{1g} modes of pristine MoS_2 [35]. The anatase phase TiO_2 was identified through the bare TiO_2 Raman spectrum corresponding to Raman bands of B_{1g}, $A_{1g}+B_{1g}$, and E_g^3 positioned at corresponding wavenumbers of 401, 520, and 640 cm^{-1}, respectively [36]. Presence of both Raman scattering in the composite samples is further proof for the formation of heterostructure between MoS_2 and TiO_2. A slight red-shift in the wavenumber was observed in the composite samples which is ascribed to the structural disorder or defects in the samples [37].

3.4 UV–Vis DRS analysis

Figure 4a shows the UV–Vis absorption spectra of the MoS_2, TiO_2, and $MoS_2@TiO_2$ core-shell heterostructure samples, respectively. It was clearly seen that all the catalysts samples exhibits their absorption in the UV–Vis region (380–410 nm). The absorption intensity was further shifted toward higher wavelength side (red-shift) for the composite sample and further covers a complete visible light region. The considerable shift in the absorption intensity of the composite sample is due to the decreasing the bandgap energy. The optical bandgap energy of the products was estimated using K–M function [38] based on the absorption intensity values and the calculated

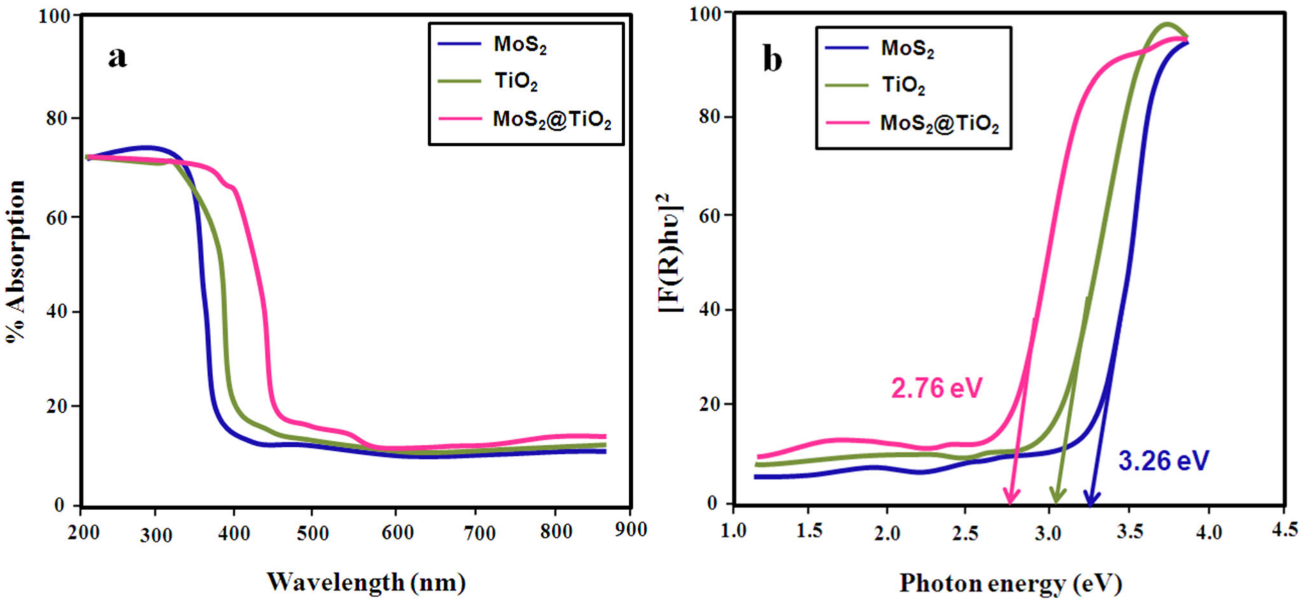

Fig. 4 UV–Vis DRS spectra of pure MoS_2, TiO_2 and $MoS_2@TiO_2$ composite catalysts. (**a**) Absorption spectra. (**b**) Kubelka–Munk model

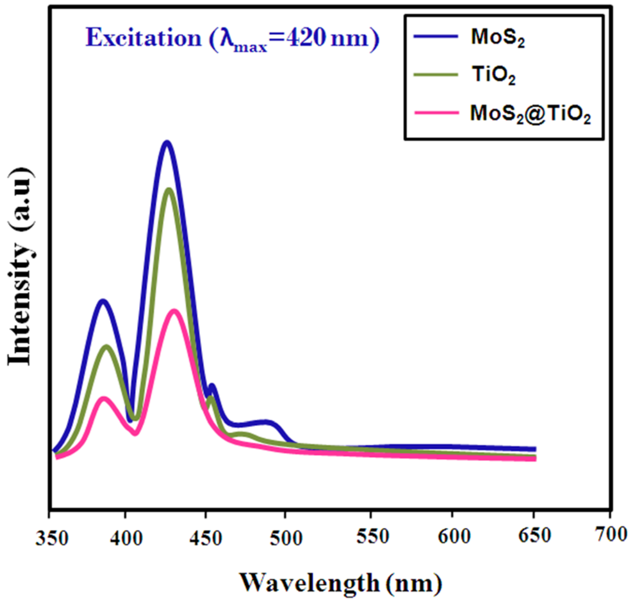

Fig. 5 Photoluminescence spectra of pure MoS_2, TiO_2 and $MoS_2@TiO_2$ composite samples

bandgap energies are 3.26, 3.06, and 2.76 eV for MoS_2, TiO_2, and $MoS_2@TiO_2$ core-shell composite samples, respectively (Fig. 4b). Decreasing the bandgap energy of $MoS_2@TiO_2$ composite than compared with bare catalyst is due to the increasing the particles size. Generally, the particle size is inversion proportional to bandgap energy. Moreover, decreasing the bandgap energy of the composite sample is due to the surface plasmon resonance (SPR) effect.

3.5 Photoluminescence spectra analysis

Figure 5 shows the room temperature PL spectra measured with wavelength region of 350–650 nm using He-Ne laser as an excited source (325 nm as excitation wavelength). The broad and sharp intensity emissions were observed in the UV (375 nm) and visible region (420–450 nm). Compared to bare sample, the $MoS_2@TiO_2$ core-shell composite shows reduced emission intensity. This could be attributed to the synergy effect in the designed $MoS_2@TiO_2$ that can hasten the spatial charge separation and suppress the electron–hole recombination, and hence increases the excitation and conversion efficiency. This is superior to developing the photocatalytic performance of the composite samples.

3.6 Nitrogen adsorption and desorption analysis

BET and BJH analysis was further carried out to know the textural properties of samples. Figure 6a and b shows the N_2 adsorption–desorption isotherm and pore size distribution of MoS_2, TiO_2 and $MoS_2@TiO_2$ samples, respectively. The curves clearly show the type IV isotherm with H3 hysteresis loop, which could be characteristics behavior of the mesoporous nature [39]. Dandelion clock heterostructures of $MoS_2@TiO_2$ possess high specific surface area (103.5 m^2/g), specific pores (33.8 nm) than compared with pure MoS_2 (88.5 m^2/g and 27.4 nm) and TiO_2 ((65.3 m^2/g and 12.4 nm). This excellent interface of heterostructures can appreciate the separation of hole and electron easily, which could increase the photodegradation of dye.

3.7 XPS analysis

The chemical component and valance state of the $MoS_2@TiO_2$ catalyst sample was investigated by XPS analysis and the relevant plot is shown in Fig. 6. The survey spectrum (Fig. 6c) clearly shows the presence of major elements such as Mo, Ti, S and O. The ideal fit for two peaks corresponding to the binding energies at 458.6 and 464.6 eV can be attributed to Ti $2p_{3/2}$ and Ti $2p_{1/2}$ core levels of Ti^{4+} cations, respectively (Fig. 6d). Figure 6e and f shows Mo 3d and S 2p spectra. The Mo $3d_{3/2}$ and Mo $3d_{5/2}$-related binding energies are positioned at 232.6 and 230.1 eV, respectively, enlightening that Mo^{4+} is the dominant oxidation state. The binding energies at 163.5 and 162.1 eV arise from S $2p_{1/2}$ and S $2p_{3/2}$ (Fig. 6f), respectively, The O 1s spectrum shows that two peaks were detected at 531.2 and 533.8 eV (Fig. 5g), which are assigned to Ti-OH bond from adsorbed water and S-O bond originating from the strong covalent interaction between TiO_2 and MoS_2.

3.8 Photocatalytic studies

In the process of photocatalytic test, the absorption ability of the catalysts was initially checked toward MO and 4-NP pollutants with equivalent absorption wavelength of 420 nm and 395 nm under visible light irradiation. UV–Vis spectrophotometer ((UV-2600SHIMADZU) has been used to monitor the absorption characteristics of the catalysts. Figure 7a–f

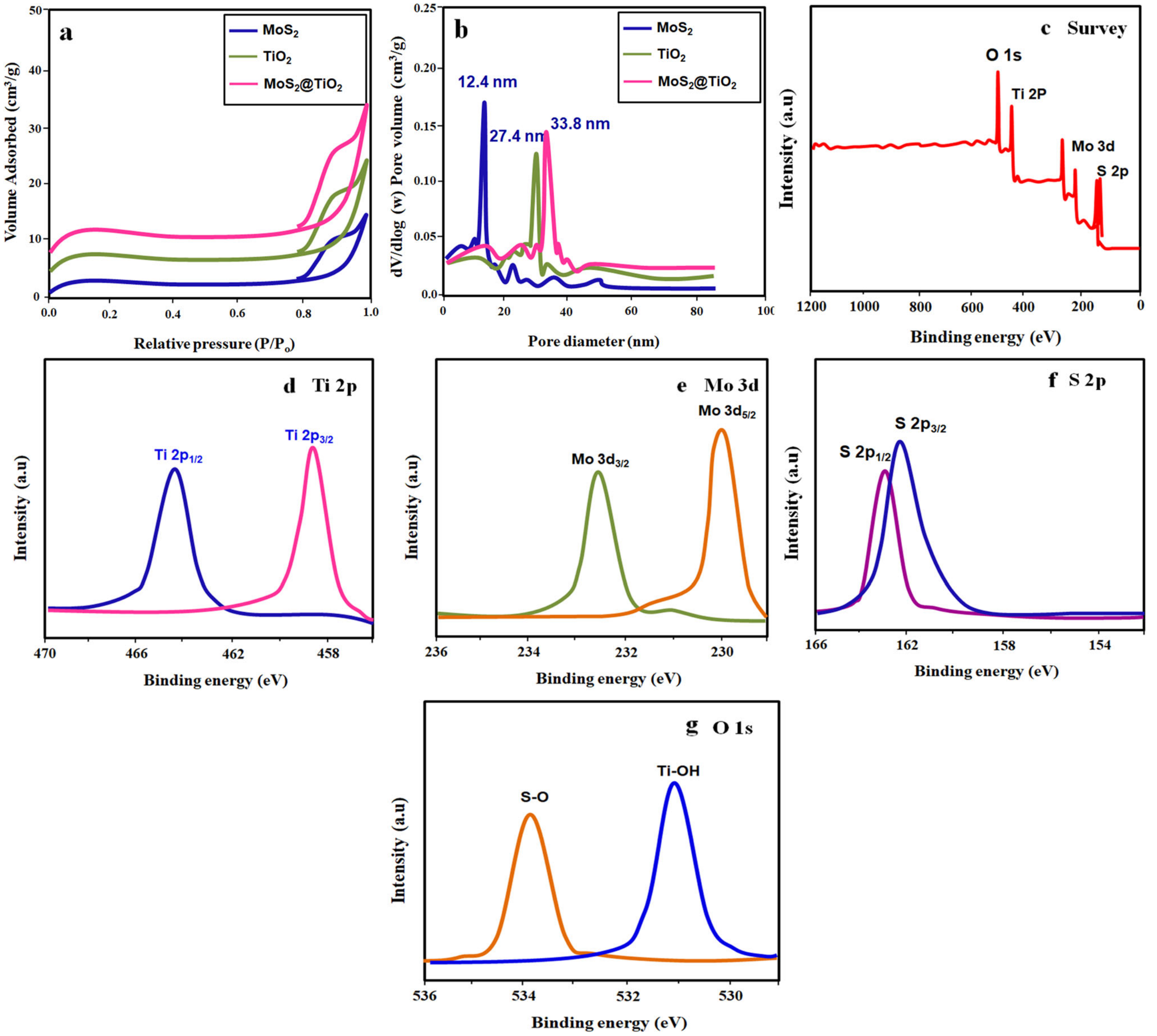

Fig. 6 (**a**) N_2 adsorption and desorption analysis MoS_2@TiO_2 and (**b**) pore size distribution; XPS of MoS_2@TiO_2 sample (**c**) survey; (**d**) Ti 2p; (**e**) Mo 3d; (**f**) S 2p and (**g**) O 1s

shows the UV absorption of MO and 4-NP dyes using MoS_2, TiO_2 and MoS_2@TiO_2 catalysts under visible light. The visible light illumination is changed from 0 to 60 min. When the visible light illumination is increased, the absorption intensity was gradually decreased. The absorption intensity was strongly reduced with the end of 60 min visible light irradiation. Decomposition test of the catalysts were evaluated for both dyes and the relevant temporal degradation profile is shown in Fig. 8a and b. The degradation efficiency is calculated based on the C/Co value [40] and MO dye efficiency was found to be 53, 63, and 86% for MoS_2, TiO_2, and MoS_2@TiO_2 core-shell composite samples, respectively (for 60 min irradiation of visible light). Similarly, the 4-NP removal efficiency was 97, 77, and 59%. In both cases, the heterojunction catalysts show high catalytic performance than compared with bare catalysts (MoS_2 and TiO_2). The catalysts were further calculated their first-order rate constants (k) [41] values and the resulting plot is shown in Fig. 8c and d. From the plot, the calculated k values are 0.0091, 0.0167, and 0.0242 min^{-1} for MoS_2, TiO_2, and MoS_2@TiO_2 core-shell composite samples, respectively (for 4-NP dye

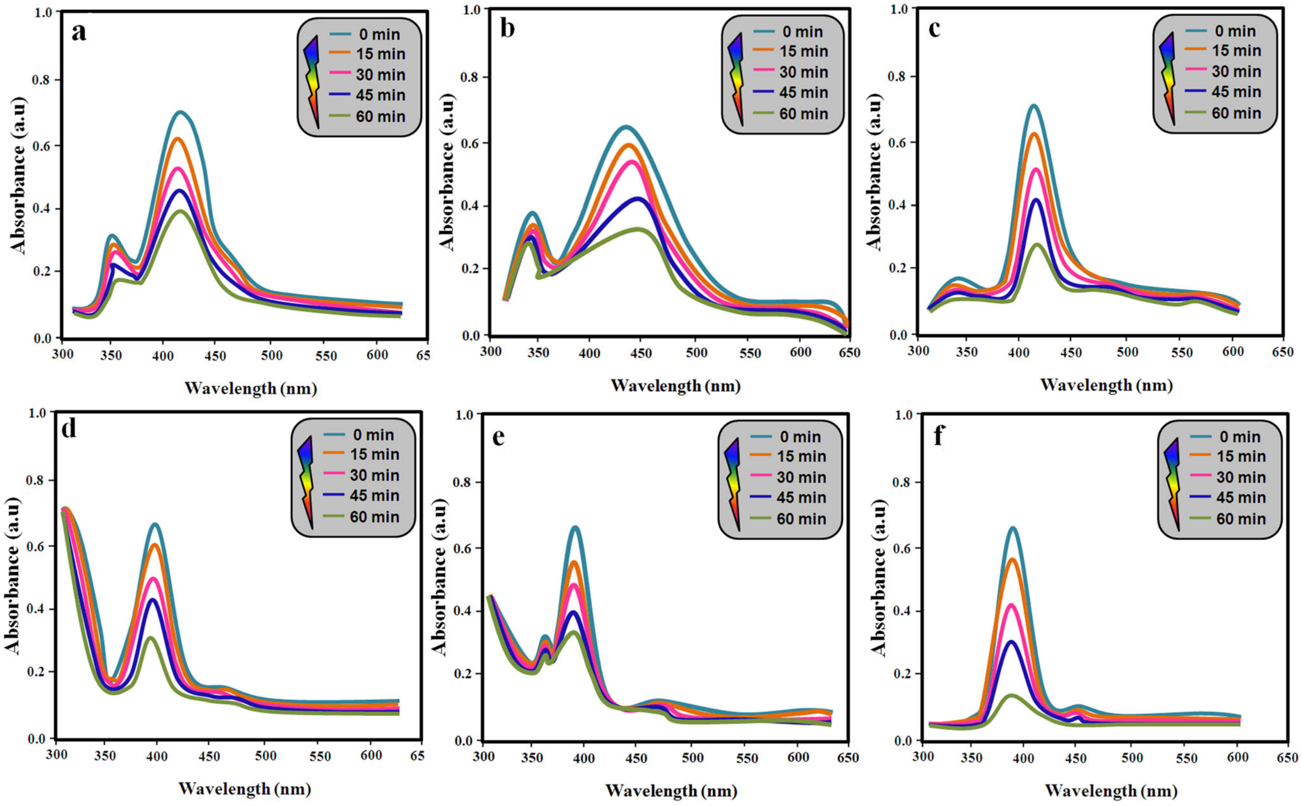

Fig. 7 UV absorption spectra of MO using (**a**) MoS_2; (**b**) TiO_2; (**c**) $MoS_2@TiO_2$; UV absorption spectra of 4-CP using (**d**) MoS_2; (**e**) TiO_2; (**f**) $MoS_2@TiO_2$ under different illumination time

under visible light). The composite sample shows high apparent constant at 26.5 times better than that of bare catalyst samples. The overall photocatalytic parameters are summarized in Table 1. Impact of scavengers within the degradation effectiveness of MO and 4-NP was moreover examined utilizing different scavengers and the related bar chart is appeared in Fig. 9a, b. The results clearly appear the degradation productivity of MO and 4-NP is 84 and 94% without any quencher. In both cases, the degradation proficiency is accomplished by t-BA than compared with other scavengers (BQ and AQ). This demonstrates that *OH radical could be a major responsive species in dye degradation. In fact, photogenerated holes are the key sources for producing the *OH radicals in the photocatalyst under visible light irradiation. Subsequently, the stability test was carried out for 5 cycles in both colors and the degradation productivity was calculated in each cycle under same experiment conditions (Fig. 9c, d). The results reveal that the prepared catalysts were highly stable. Particularly, the composite catalyst has no significant loss within the degradation efficiency. The schematic illustration of the photocatalytic mechanism and photoinduced electrons and holes separate by {101} and {001} facets of anatase TiO_2 as shown in Fig. 10a and b. Under visible light irradiation, electrons and hole pairs were produced on MoS_2 of CB and VB, respectively. while, the electron are back into the conduction band of TiO_2 due to the similar energy levels [42]. With the presence of visible light, O_2 molecules react with the H^+ ions and electrons on the CB of $MoS_2@TiO_2$ to produce H_2O_2, and the resulting H_2O_2 can further react with electrons to generate *OH. Due to the more positive potential of OH/OH^* than that the VB potential of TiO_2, the *OH radicals cannot be produced by the oxidation of H_2O with holes. The holes will directly react with methyl orange molecules adsorbed on the $MoS_2@TiO_2$ surface. In addition, due to the more negative potential of CB for TiO_2, the photoexcited electrons can quickly transfer from the CB of TiO_2 to that of MoS_2, and the holes on the VB of TiO_2 will move to the VB of MoS_2. The reaction mechanism of the heterojunction catalyst toward MO dyes is as follows:

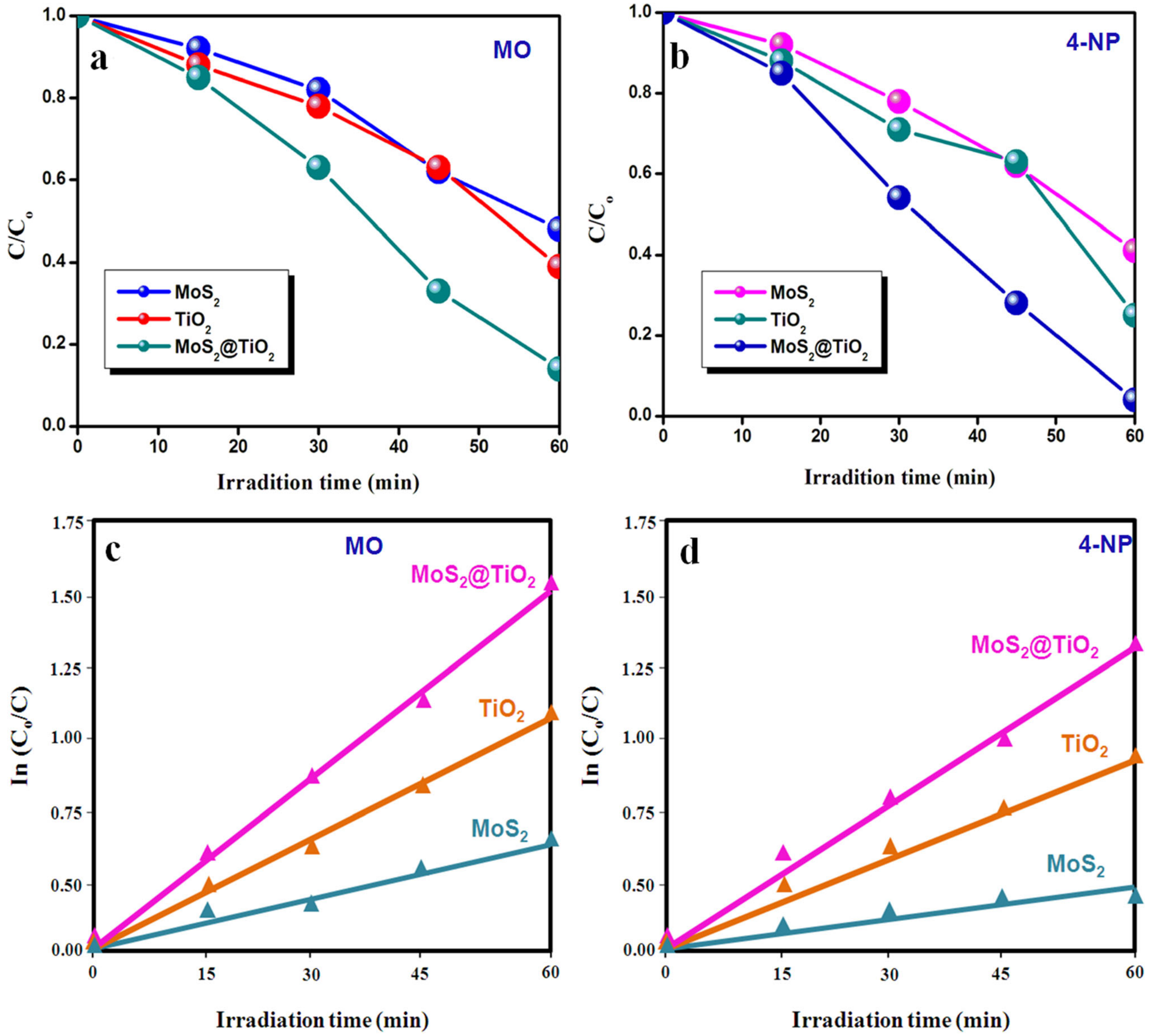

Fig. 8 Temporal degradation profile of (**a**) MO; (**b**) 4-NP; Kinetic plot of (**c**) MO; (**d**) 4-NP for all the catalyst powders

Table 1 Photocatalytic parameters of pure MoS_2, TiO_2 and MoS_2@TiO_2 composite samples

Samples	Bandgap (eV)	Rate constant of MO		Rate constant of 4-NP		Degradation efficiency at 60 min	
		K (h^{-1})	R^2	K (h^{-1})	R^2	MO	4-NP
MoS_2	3.26	0.0081	0.945	0.0091	0.958	53	59
TiO_2	3.06	0.0124	0.968	0.0167	0.947	63	77
MoS_2@TiO_2	2.76	0.0161	0.995	0.0242	0.978	86	97

$$MoS_2@TiO_2\left(h^+\right) + H_2O \rightarrow H^+ + {}^*OH \quad (1)$$

$$^*O_2^- + MO \rightarrow \text{degraded products (minor)} \quad (2)$$

$$^*OH + MO \rightarrow \text{degraded products (minor)} \quad (3)$$

$$h^+ + MO \rightarrow \text{degraded products (minor)} \quad (4)$$

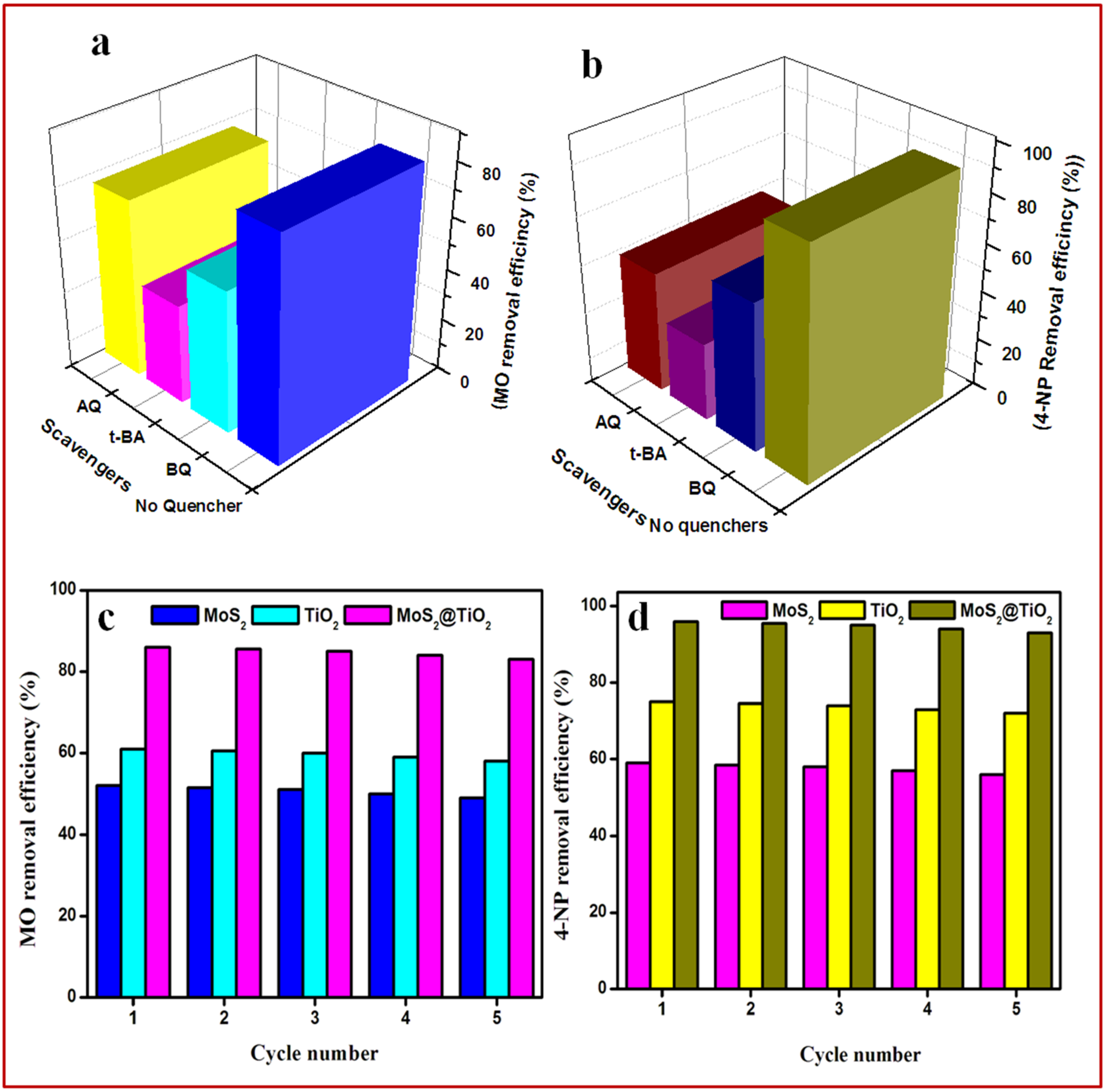

Fig. 9 Effect of various scavenger on the removal efficiency of (**a**) MO; (**b**) 4-NP for all the catalysts; cycling stability test of (**c**) MO; (**d**) 4-NP pollutants

In addition, redistribution of electrons and holes can effectively restrain the electron–hole recombination. The heterojunction structure of MoS$_2$@TiO$_2$ sample is thus beneficial for the recombination of electron–hole pairs, which results in high photocatalytic performance. Preventing the recombination of electron–hole pairs and narrowing the bandgap energies are crucial role to improve the photocatalytic performance. The photoresponse ability of the same catalysts was determined using chronoamperometric measurements under potentiostatic control at 1.23 VRHE, as shown in Fig. 10b. In general, the photoelectrodes exhibited a prompt photoresponse under intermittent irradiation with high reproducibility during numerous ON/OFF cycles, as well as good electrochemical stability during continuous irradiation for 1 h. It is noteworthy that the photocurrent density results again prove that MoS$_2$@TiO$_2$ catalyst

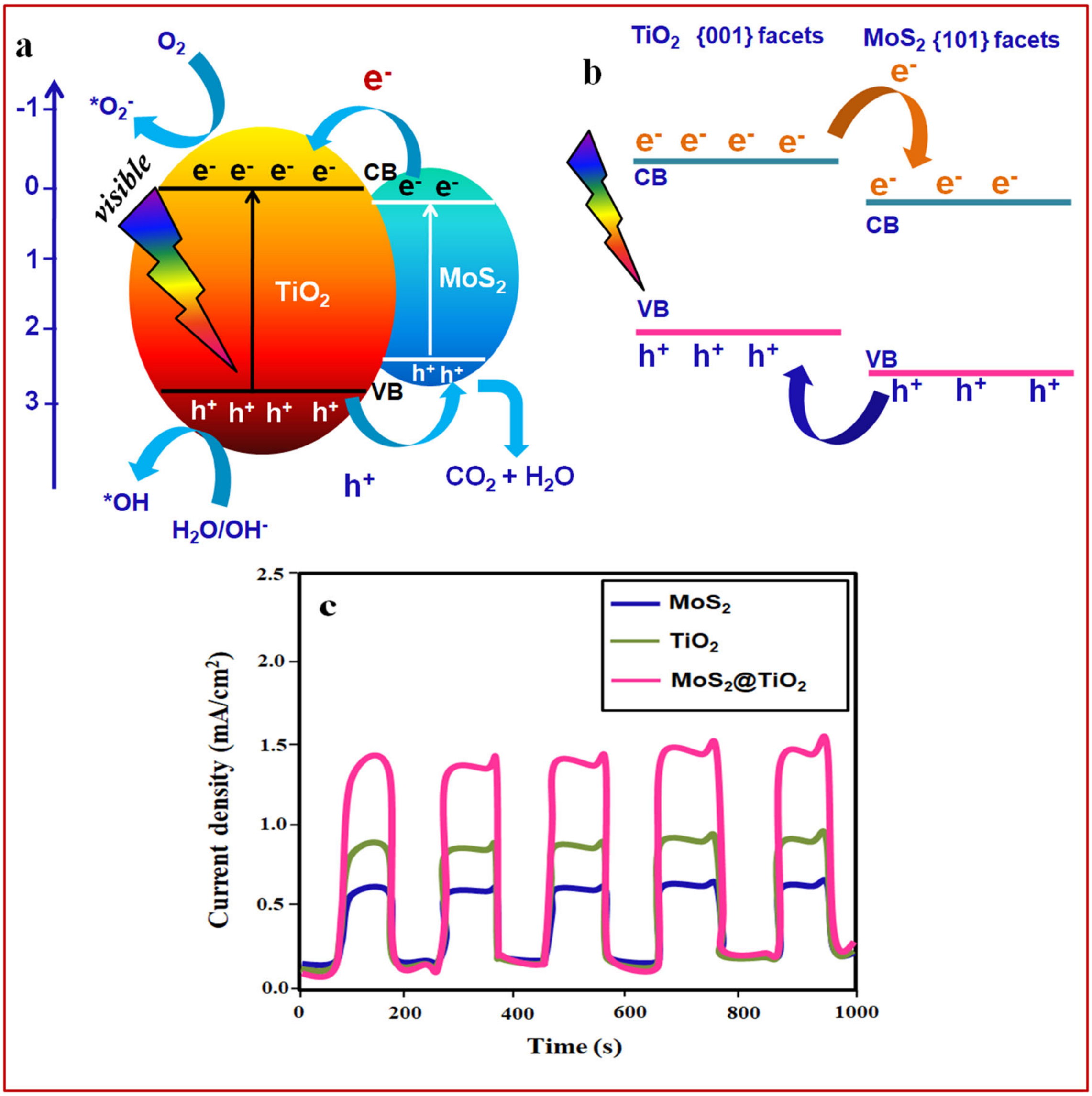

Fig. 10 (**a**) Schematic diagram of carries exchange in the $MoS_2@TiO_2$ heterostructure; (**b**) photoinduced electrons and holes separate by {101} and {001} facets of anatase TiO_2; (**c**) time-dependent photocurrent density of all the catalyst samples

shows high photocurrent response, which is consistent with the photocatalytic degradation results. Hence, the photoelectrochemical results suggest that $MoS_2@TiO_2$ catalyst produced the high photoresponse than compared with pure MoS_2 and TiO_2 catalysts, respectively.

4 Conclusions

In summary, a dandelion clock, core-shell $TiO_2@MoS_2$ composite photocatalysts with visible light activity were fabricated via a one-step hydrothermal method. In the process of the photocatalytic experiment, MO and 4-NP pollutants were the primary products over the $TiO_2@MoS_2$ heterojunction composites. The results show that the pure TiO_2 and MoS_2 demonstrate a poor photocatalytic activity based on its high electron–hole recombination. The maximum yields of MO and 4-NP are in $TiO_2@MoS_2$ heterojunction composite, whose efficiency was 97% and 86%, respectively. The improved photocatalytic activity of $TiO_2@MoS_2$ heterojunction composite could be owing to the high efficiency separation of photogenerated electron–hole pairs, intense response to visible light and the narrowed bandgap. Hence, this work shows that sulfide can enhance the photocatalytic activity of TiO_2 in photocatalytic degradation of 4-NP dye with great potential.

References

1. A. Fujishima, K. Honda, Electrochemical photolysis of water at a semiconductor electrode. Nature **238**, 37–38 (1972)
2. S. Bai, L. Wang, X. Chen, J. Du, Y. Xiong, Chemically exfoliated metallic MoS_2 Nanosheets: A promising supporting co-catalyst for enhancing the Photocatalytic performance of TiO_2 nanocrystals. Nano Res. **8**, 175–183 (2015)
3. U. Krishnan, M. Kaur, K. Singh, G. Kaur, P. Singh, M. Kumar, A. Kumar, MoS_2/Ag nanocomposites for electrochemical sensing and photocatalytic degradation of textile pollutant. J. Mater. Sci. Mater. Electron. **30**, 3711–3721 (2019)
4. U. Krishnan, M. Kaur, G. Kaur, K. Singh, A.R. Dogra, M. Kumar, A. Kumar, MoS2/ZnO nanocomposites for efficient photocatalytic degradation of industrial pollutants. Mater. Res. Bull. **111**, 212–221 (2019)
5. A.K.G. Kaur, B. Singh, P. Singh, K. Singh, A. Thakur, M. Kumar, R. Bala, ron Disulfide (FeS_2): A promising material for removal of industrial pollutants. Chemistryselect **2**, 2166–2173 (2017)
6. Q. Liang, Z. Li, X. Yu, Z.H. Huang, F. Kang, Q.H. Yang, Macroscopic 3D porous graphitic carbon nitride monolith for enhanced Photocatalytic hydrogen evolution. Adv. Mater. **27**, 4634–4639 (2015)
7. I. Dincer, Green methods for hydrogen production. Int. J. Hydrog. Energy **37**, 1954–1971 (2012)
8. R. Li, Latest Progress in hydrogen production from solar water splitting via photocatalysis, photoelectrochemical, and photovoltaic-photoelectrochemical solutions. Chin. J. Catal. **38**, 5–12 (2017)
9. T. Banerjee, A. Mukherjee, Overall water splitting under visible light irradiation using nanoparticulate RuO_2 loaded Cu_2O powder as photocatalyst. Energy Procedia **54**, 221–227 (2014)
10. D. Ravelli, D. Dondi, M. Fagnoni, A. Albini, Photocatalysis. A multi-faceted concept for green chemistry. Chem. Soc. Rev. **38**, 1999–2011 (2009)
11. D. Bahnemann, Photocatalytic water treatment: Solar energy applications. Sol. Energy **77**, 445–459 (2004)
12. P.V. Kamat, Meeting the clean energy demand: Nanostructure architectures for solar energy conversion. J. Phys. Chem. C. **111**, 2834–2860 (2007)
13. B. Dunn, H. Kamath, J.-M. Tarascon, Electrical energy storage for the grid: A battery of choices. Science **334**, 928–935 (2011)
14. M. Armand, J.M. Tarascon, Building better batteries. Nature **451**, 652–657 (2008)
15. M.D. Slater, D. Kim, E. Lee, C.S. Johnson, Sodium-Ion Batteries. Adv. Funct. Mater. **23**, 947–958 (2013)
16. H. Pan, Y.-S. Hu, L. Chen, Room-temperature stationary sodium-ion batteries for large-scale electric energy storage. Energy Environ. Sci. **6**, 2338–2360 (2013)
17. D.-D. Zhu, J.L. Liu, S.Z. Qiao, Recent advances in inorganic heterogeneous electrocatalysts for reduction of carbon dioxide. Adv. Mater. **28**, 3423–3452 (2016)
18. Y. Tang, Z. Jiang, G. Xing, A. Li, P.D. Kanhere, Y. Zhang, T.C. Sum, S. Li, X. Chen, Z. Dong, Z. Chen, Efficient ag@ AgCl cubic cage photocatalysts profit from ultrafast plasmon-induced electron transfer processes. Adv. Funct. Mater. **23**, 2932–2940 (2013)
19. J. Mao, M. Ge, J. Huang, Y. Lai, C. Lin, K. Zhang, K. Meng, Y. Tang, Constructing multifunctional MOF@rGO hydro-/aerogels by the self-assembly process for customized water remediation. J. Mater. Chem. A **5**, 11873–11881 (2017)
20. M. Sumathi, A. Prakasam, P.M. Anbarasan, High capable visible light driven photocatalytic activity of WO_3/g-C_3N_4 hetrostructure catalysts synthesized by a novel one step microwave irradiation route. J. Mater. Sci. Mater. Electron. **30**, 3294–3304 (2019)
21. M. Sumathi, A. Prakasam, P.M. Anbarasan, Fabrication of hexagonal disc shaped nanoparticles g-C_3N_4/NiO heterostructured nanocomposites for efficient visible light photocatalytic performance. J. Clus. Sci. **30**, 757–766 (2019)
22. M. Parthibavarman, S. Sathishkumar, M. Jayashree, R. BoopathiRaja, Microwave assisted synthesis of pure and Ag doped SnO_2 quantum dots as novel platform for high photocatalytic activity performance. J. Clus. Sci. **30**, 351–363 (2019)
23. M. Parthibavarman, S. Sathishkumar, S. Prabhakaran, M. Jayashree, R. BoopathiRaja, High visible light-driven photocatalytic activity of large surface area Cu doped SnO_2 nanorods synthesized by novel one-step microwave irradiation method. J. Iran. Chem. Soc. **15**, 2789–2801 (2018)
24. L. Zhang, Z. Xing, H. Zhang, Z. Li, X. Wu, X. Zhang, Y. Zhang, W. Zhou, High thermo-stable ordered mesoporous SiO_2–TiO_2 coated circulating-bed biofilm reactor for unpredictable photocatalytic and biocatalytic performance. Appl Catal B **180**, 521–529 (2016)
25. S. Pan, X. Liu, M. Guo, S. Yu, H. Huang, H. Fan, G. Li, Engineering the intermediate band states in amorphous Ti^{3+}-doped TiO_2 for hybrid dye-sensitized solar cell applications. J. Mater. Chem. A **3**, 11437–11443 (2015)

26. Z. Fan, F. Meng, M. Zhang, Z. Wu, Z. Sun, A. Li, Solvothermal synthesis of hierarchical TiO_2 nanostructures with tunable morphology and enhanced photocatalytic activity. Appl. Surf. Sci. **360**, 298–305 (2016)
27. Z. Fan, F. Meng, J. Gong, H. Li, A. Li, Growth mechanism and photocatalytic activity of chrysanthemum-like anatase TiO_2 nanostructures. Ceram. Int. **42**, 6282–6287 (2016)
28. R. Qin, F. Meng, M.W. Khan, B. Yu, H. Li, Z. Fan, J. Gong, Fabrication and enhanced photocatalytic property of TiO2-ZnO composite photocatalysts. Mater. Lett. **240**, 84–87 (2019)
29. K. Guo, Z. Liu, J. Han, X. Zhang, Y. Li, T. Hong, C. Zhou, Higher-efficiency photoelectrochemical electrodes of titanium dioxide-based nanoarrays sensitized simultaneously with plasmonic silver nanoparticles and multiple metal sulfides. J. Power Sources **285**, 185–194 (2015)
30. G. Moon, W. Kim, A.D. Bokare, N. Sung, W. Choi, Solar production of H_2O_2 on reduced graphene oxide–TiO_2 hybrid photocatalysts consisting of earth-abundant elements only. Energy Environ. Sci. **7**, 4023–4028 (2014)
31. W. Li, F. Wang, Y. Liu, J. Wang, J. Yang, L. Zhang, A.A. Elzatahry, D. Al-Dahyan, Y. Xia, D. Zhao, General strategy to synthesize uniform mesoporous TiO_2/graphene/mesoporous TiO_2 sandwich-like nanosheets for highly reversible lithium storage. Nano Lett. **15**, 2186–2193 (2015)
32. D. Gopalakrishnan, D. Damien, M.M. Shaijumon, MoS_2 quantum dot-interspersed exfoliated MoS_2 nanosheets. ACS Nano **8**, 5297–5303 (2014)
33. Q. Liu, X. Li, Q. He, A. Khalil, D. Liu, T. Xiang, X. Wu, L. Song, Gram-scale aqueous synthesis of stable few-layered 1T-MoS_2: Applications for visible-light-driven photocatalytic hydrogen evolution. Small. **11**, 5556–5564 (2015)
34. M. Parthibavarman, K. Vallalperuman, S. Sathishkumar, M. Durairaj, K. Thavamani, A novel microwave synthesis of nanocrystalline SnO_2 and its structural optical and dielectric properties. J. Mater. Sci. Mater. Electron. **25**, 730–735 (2014)
35. M. Shen, Z. Yan, L. Yang, P. Du, J. Zhang, B. Xiang, MoS_2 nanosheet/TiO_2 nanowire hybrid nanostructures for enhanced visible-light photocatalytic activities. Chem. Commun. **50**, 15447–15449 (2014)
36. H. Li, Y. Wang, G. Chen, Y. Sang, H. Jiang, J. He, X. Li, H. Liu, Few-layered MoS_2 nanosheets wrapped ultrafine TiO_2 nanobelts with enhanced photocatalytic property. Nanoscale. **8**, 6101–6109 (2016)
37. Q. Xiang, J. Yu, M. Jaroniec, Synergetic effect of MoS_2 and graphene as co catalysts for enhanced photocatalytic H_2 production activity of TiO_2 nanoparticles. J. Am. Chem. Soc. **134**, 6575–6578 (2012)
38. M. Parthibavarman, M. Karthik, P. Sathishkumar, R. Poonguzhali, Rapid synthesis of novel Cr-doped WO_3 nanorods: An efficient electrochemical and photocatalytic performance. J. Iran. Che. Soc. **15**, 1419–1430 (2018)
39. R. BoopathiRaja, M. Parthibavarman, Hetero-structure arrays of $MnCo_2O_4$ nanoflakes@ nanowires grown on Ni foam: Design, fabrication and applications in electrochemical energy storage. J. Alloy. Compd. **811**, 152084 (2019)
40. X. Yan, K. Liu, W. Shi, Facile synthesis of CdS/$MnWO_4$ heterojunction with enhanced visible-light-driven photocatalytic activity and mechanism investigation. Colloids Surf. A Physicochem. Eng. Aspects **520**, 138–145 (2017)
41. J. Zhang, L. Huang, Z. Lu, Z. Jin, X. Wang, G. Xu, E. Zhang, H. Wang, Z. Kong, J. Xi, Z. Ji, Crystal face regulating MoS_2/TiO_2 (001) heterostructure for high photocatalytic activity. J. Alloy. Compd. **688**, 840–848 (2016)
42. R. Asahi, T. Morikawa, T. Ohwaki, K. Aoki, Y. Taga, Visible-light photocatalysis in nitrogen-doped titanium oxides. Science **293**, 269–271 (2001)